UC Irvine

Title

Numerical evaluation of high-energy, laser-Compton x-ray sources for contrast enhancement and dose reduction in clinical imaging via gadolinium-based K-edge subtraction.

Permalink

Journal

Authors

Reutershan, Trevor
Effarah, Haytham
Lagzda, Agnese
et al.

Publication Date

DOI

Numerical evaluation of high-energy, laser-Compton X-ray sources for contrast enhancement and dose reduction in clinical imaging via gadolinium-based K-edge subtraction

Trevor Reutershan[1,2], **Haytham H. Effarah**[1,2], **Agnese Lagzda**[3], **C. P. J. Barty**[1,2,3,*]

[1]Department of Physics and Astronomy, University of California – Irvine, CA, 92617

[2]Beckman Laser Institute and Medical Clinic, University of California – Irvine, CA, 92697

[3]Lumitron Technologies, Inc., 5201 California Ave, Suite 100, Irvine, CA, 92617, USA

Abstract

Conventional X-ray sources for medical imaging utilize bremsstrahlung radiation. These sources generate large bandwidth X-ray spectra with large fractions of photons that impart dose but do not contribute to image production. X-ray sources based on laser-Compton scattering can have inherently small energy bandwidths and can be tuned to low dose-imparting energies, allowing them to take advantage of atomic K-edge contrast enhancement. This paper investigates the use of gadolinium-based K-edge subtraction imaging in the context of mammography using a laser-Compton source through simulations quantifying contrast and dose in such imaging systems as a function of laser-Compton source parameters. Our simulations indicate that a KES image generated with a 0.5% bandwidth (FWHM) laser-Compton X-ray source can obtain an equal contrast to a bremsstrahlung image with only 3% of the dose.

1. Introduction

The clinical benefit of diagnostic X-ray imaging is ultimately limited by the radiation dose imparted upon a patient. Conventional X-ray sources utilize the collision of electrons with metals to produce a broadband spectrum of X-rays with a maximum X-ray energy related to the energy of the incident electrons and line radiation characteristic of the metal. This *bremsstrahlung* approach to producing X-rays for diagnostic medical imaging produces large quantities of low-energy X-rays that cannot penetrate through the human body and only serve to increase dose imparted upon a patient without any contribution to image acquisition.

In the case of mammography, the presence of these non-contributing X-rays increases the mean glandular dose (MGD) to breast tissue unnecessarily, causing an increased, albeit marginal, lifetime risk of developing breast cancer. Additionally, the diagnostic power of mammography is limited by its ability to identify potentially cancerous lesions amid the backdrop of benign breast tissue structures. This diagnostic power drastically decreases with

---

*cbarty@uci.edu .

increased breast density [1], which leads to frequent inconclusive mammograms and the need for follow-up with alternative imaging modalities. The low positive predictive value of mammography, especially in women with dense breasts, leads to psychological/financial burden on patients and administrative/financial burden on healthcare providers. While the benefits of breast cancer screening outweigh the risks for women over the age of 40 [2], the radiation lifetime risk and diagnostic limitations of mammography limit its utility. Even with widespread screening, breast cancer is still the second most common cause of cancer death in women. Improvements in the diagnostic power of mammograms and reductions in MGD are direly needed.

Contrast-enhanced digital mammography (CEDM) seeks to improve the diagnostic quality of mammography by taking advantage of the K-edge of elements contained in image contrast agents, namely iodine. CEDM, like other forms of K-edge subtraction (KES) imaging, requires the acquisition of images using X-ray energies above and below the binding energy of the K-shell electron of an image contrast agent. At energies just above and below the K-edge of the element contained in the contrast agent, the relative attenuation of X-rays through biological matter is nearly constant, while the relative attenuation of X-rays through the contrast agent is selectively enhanced. This differential effect can help isolate regions that preferentially retain image contrast agents, like the leaky microvasculature commonly found around cancerous lesions. CEDM has shown increased diagnostic power over traditional mammography and has even been demonstrated to have comparable diagnostic power to 3D contrast-enhanced breast MRI [3]. However, the dependence of CEDM on conventional X-ray sources increases the radiation dose imparted on patients relative to traditional mammography and does not use the full potential of the differential enhancement of the contrast agent's K-edge.

Quasi-monochromatic X-ray sources have shown promising preliminary results as potential solutions to the limitations of conventional X-ray sources in KES imaging techniques like CEDM. These X-ray sources have small energy bandwidths, eliminating the presence of unwanted dose and improving the signal-to-noise ratio of injected contrast agents. To date, synchrotron radiation and laser-Compton scattering (LCS), sometimes also referred to as inverse Compton scattering (ICS), radiation are two alternative X-ray generation techniques that have been shown to be capable of producing quasi-monochromatic X-rays at fluxes acceptable for human radiographic imaging [4–6].

Several studies that employed synchrotron radiation have shown superior mammography to conventional sources at fractions of the MGD, and have even shown opportunities for high resolution breast tomography with doses less than those of conventional two-projection mammography [7]. While these results are promising, the facility-scale of synchrotron sources makes them financially and geographically impractical for widespread use in breast cancer screening and breast cancer diagnosis. LCS sources produce quasi-monochromatic X-rays with larger attainable energies than synchrotron sources, and because of their mode of operation, they are capable of being scaled down in size and cost, providing a clear path towards routine clinical use.

Research regarding KES imaging using conventional X-ray, synchrotron, and early LCS sources has been limited to elements with K-edge energies between 30–40 keV such as iodine and experiments have been performed using filters as opposed to direct energy tuning [8, 9]. High-Z elements have K-edge transitions at higher energies, thereby giving the potential to increase image quality and decrease dose beyond what has been previously studied. Among these high-Z elements is gadolinium, which is routinely used as contrast for MRI breast imaging studies.

To investigate this new energy scale, this paper aims to quantify these benefits using gadolinium as a contrast agent in a series of computer simulations under clinically relevant conditions. As the number of LCS sources capable of performing experiments increases, this study will be a valuable tool for future experimental design. As the choice of X-ray energy and bandwidth are selectable in a laser-Compton source, the image quality and dose will be functions of these attributes. The authors evaluate how to configure a LCS source to perform gadolinium-based K-edge subtraction imaging and quantify the extent to which the unique properties of laser-Compton X-rays can translate into the acquisition of images with lower dose and higher diagnostic power when compared to traditional X-ray sources.

2.   K-Edge Imaging Using Laser-Compton Sources

2.1   Laser-Compton Scattering

Laser-Compton sources produce X-rays via scattering of laser photons off relativistic electrons. In the rest frame of the electron, this process is simply traditional Compton scattering, where the energy of the scattered photon is less than or equal to that of the incoming photon. When transformed to the lab frame of the observer, the energy of the scattered photon is upshifted into the X-ray regime. Because the electron energies required to produce X-ray radiation are achievable by current linear accelerator technology, LCS sources are significantly compact. Moreover, LCS X-ray sources offer the potential for small energy bandwidths and small effective source sizes that can provide high-precision imaging techniques not afforded by bremsstrahlung sources. The energy of a Compton-scattered X-ray, E_γ, emerging from a collision with a relativistic electron is given by [10, 11]:

$$E_\gamma = \frac{\gamma - \sqrt{\gamma^2 - 1}\cos\phi}{\gamma - \sqrt{\gamma^2 - 1}\cos\theta + k_0\lambda_c(1 - \cos\theta\cos\phi + \cos\psi\sin\theta\sin\phi)}E_L \qquad (1)$$

Where γ is the electron's Lorentz factor, K_0 is the wave number of the incident photon, λ_c is the reduced Compton wavelength of the electron, E_L is the incident photon energy, ϕ is the angle between the incident electron and photon, θ is the angle between the incident electron and scattered photon, and ψ is the angle between incident and scattered photons. In the simplified case of a head on collision, where $\phi = \pi$, for small observation angles, where $\sin\theta \approx \theta$, the equation can be approximated to be

$$E_\gamma \approx \frac{4\gamma^2}{1 + \gamma^2\theta^2 + 4\gamma k_0\lambda_c}E_L. \qquad (2)$$

LCS sources have been designed to produce fluxes greater than 10^{12} photons per second with on-axis bandwidths of 10^{-3} (ΔE/E, FWHM) [12, 13]. The flux at MeV energies vastly exceeds the capabilities of synchrotrons as well as rotating anodes used for medical imaging. As the sample source for image analysis, we use a currently-under-construction, high-flux, narrow-band LCS source based on US patent #US9706631B2 that is anticipated to have the parameters listed in Table 1. This particular laser-Compton architecture theoretically has the ability to produce on-axis X-ray bandwidths of as small as 0.1% FWHM [11, 13].

In a typical LCS spectrum, half of the Compton-scattered X-rays are contained within a $1/\gamma$ cone. The maximum X-ray energy corresponds to the energy of X-rays in perfect backscatter, also referred to as the Compton edge (CE). The general energy profile of an LCS X-ray spectrum is dependent on the specific features (energy, shape function, emittance, etc.) of both the electron beam and the laser beam, and how these two beams overlap in time and space within the interaction region. This interaction leads to a spatially dependent energy spectrum and can most generally be described by the following equation for the energy-angle X-ray spectrum [10, 14, 15]:

$$\frac{dN}{d\Omega\, d\omega} = \int \frac{d\sigma}{d\Omega} \delta\left(\omega - \omega_1 \frac{\kappa_l}{\kappa}\right)\left(1 - \boldsymbol{\beta} \cdot \frac{c\,\boldsymbol{k}}{\omega_1}\right) n_l(x_\mu) n_e(x_\mu) d^4 x_\mu. \tag{3}$$

Here, n_l and n_e are the incident light and electron densities, respectively, as functions of the electron 4-position x_μ, c is the speed of light, $\boldsymbol{k}$ is the incident light wavenumber, and $\boldsymbol{\beta}$ is the electron velocity. The differential cross-section, $d\sigma/d\Omega$, is interpreted as the interaction probability of the two overlapping densities and is described by the Lorentz-boosted Klein-Nishina formula [16]. The delta function appropriately chooses the scattered X-ray frequencies, ω, from the incident light frequency, ω_1, and the ratio of the electron light-cone variables with respect to the incident photons, k_l, and the scattered photons, k, as described in [15]. Figure 1 graphically illustrates an interaction zone where a laser envelope interacts with an electron bunch and includes sample X-ray spectra for the LCS source used for the simulation studies.

Adjustment of the viewing angle allows for tuning of the bandwidth. This can be performed using an aperture to block the lower energy and lower intensity photons that arise further away from the center of the spectrum according to Eq. (2). Five viewing angles were used to select bandwidth in this study. The 1, 1.5, 2, 3.5 and 5 mrad apertures yielded ΔE/E FWHM bandwidths (BW) of approximately 0.5%, 1%, 2%, 6% and 11%, respectively. Because linearly polarized laser light is assumed, the flux of the source is polar with higher fluxes in the vertical direction compared to the horizontal direction (laser polarization direction). On the other hand, the mean energy contours are circular as the energy of the scattered photons are predominantly determined by Eq. (2), with decreasing energy as you move away from the center axis.

Due to the tunable narrow bandwidth capabilities of LCS sources, there is motivation for subtraction imaging schemes in a wide range of applications. For this paper, we focus on applying such sources to KES and mammography. While this analysis is based on the

predicted performance of a source currently being developed by Lumitron Technologies, Inc., it is valid for any architecture when details about the X-ray source are available.

2.2 K-Edge Subtraction Imaging

K-edge subtraction imaging is a process with discussion for use in medical diagnosis dating back to the 1940's [17–20] that takes advantage of the large change in attenuation cross section when a 1s electron absorbs radiation (see Figure 2[c] for an example K-edge attenuation coefficients of various metals). In theory, if two images are taken using energies of photons near the K-edge of a contrast element, distracting background features can be subtracted away leaving enhancement at the area of interest. The subtraction may be performed on the transmission images, log-attenuation (absorption) images, or any post-processed version of the two. To keep the analysis simple for this paper, we perform the background subtraction on the transmission images (Eq. 4a) for section 3 to verify the photon counts between Monte Carlo and Beer-Lambert computational methods, and the log-attenuation (Eq. 4b) for section 4 when comparing KES to conventional absorption images.

$$S = C_b - C_a \tag{4a}$$

$$S = \log C_a - \log C_b \tag{4b}$$

Here, C_a and C_b are the photon counts at the detector for the above and below K-edge images, respectively. S represents the KES signal, which is calculated for every pixel of the image. When energies near the K-edge of an element are used, these operations will effectively eliminate the background leaving only the signal corresponding to the contrast agent. The choice of order of subtraction (below minus above) is chosen based on the assumption that the contrast agents have a higher attenuation than the background tissue/material, therefore leaving a higher or brighter signal at the region of interest (ROI).

Monoenergetic X-rays would be ideal to use for KES imaging. Currently, the available commercial systems that are capable of dual-energy imaging use conventional bremsstrahlung radiation [21–23]. An LCS source would provide the low bandwidths and large fluxes necessary to perform quality KES imaging, while being compact enough for a clinical setting. The purpose of this paper is to investigate the feasibility of KES mammography using a LCS source and gadolinium as a contrast agent in a projection configuration, as well as explore the advantages and tradeoffs of flux and bandwidth compared to other conventional sources.

2.3 Dose and Contrast Optimization

To understand how the dose and contrast change with energy, we propose two figure of merits that minimizes the dose while simultaneously maximizing the contrast or photon counting statistics. Under charged particle equilibrium (CPE), the dose, D, for a uniform X-ray beam incoming on a sufficiently thin material can be approximated by [24]

$$D = E\phi\left(\frac{\mu_{en}(E)}{\rho}\right) \tag{5}$$

where ϕ is the incoming photon fluence with energy E and (μ_{en}/p) is the energy dependent mass absorption coefficient.

The image can only be created using photons that pass through the object and reach the detector. To quantify this, it is simply a measure of the fraction of photons, f, that get attenuated through the material according to the Beer-Lambert law.

$$f = e^{-\mu(E)l} \tag{6}$$

Here, μ is the linear attenuation coefficient and l is the path length of the material. An appropriate figure of merit would be the dose area product per transmitted photon (DAPT) calculated as the dose divided by the incoming photon fluence and the attenuation. The resulting quantity can be interpreted as the dose per *exiting* photon fluence as a function of photon energy.

$$DAPT \stackrel{\text{def}}{=} \frac{D}{\phi f} = E\left(\frac{\mu_{en}(E)}{\rho}\right)e^{\mu(E)l} \tag{7}$$

Minimization of this quantity would yield the optimized simultaneous scenario of minimized dose and maximized non-interaction with the background medium.

Monte Carlo (MC) simulation was used to verify the theoretical DAPT. All Monte Carlo (MC) experiments in this study were performed using TOPAS version 3.5 [25] whose backend is the Geant4 Simulation Toolkit version 10.06.p01 developed and maintained by CERN [26]. A sufficiently thin cylindrical water phantom of radius 5 cm and thickness 1 mm was used. A simulation was run using monoenergetic photons in the energy range from 10 keV to 1 MeV in 10 keV steps. Each simulation consisted of 1 million particles. The dose was monitored as well as exiting photon fluence from the phantom to calculate the DAPT.

The results of dose optimization can be found in Figure 2(a). The Monte Carlo curve was obtained by dividing the total dose imparted to the phantom by the exiting flux of photons as measured by a surface track counter 1 mm behind the phantom. The theoretical curve was constructed by the DAPT equation described above. The theoretical result matches well with the MC result until about 225 keV when the two curves diverge from each other and the theoretical DAPT overpredicts the one from MC. This difference is expected since at high X-ray energies, there is a build-up factor that needs to be accounted for where the peak dose depth increases with increasing energy because transient CPE is not attained until larger depths.

Figure 2(a) identifies the optimal energy range for medical imaging to be between 45 keV and 90 keV. This corroborates prior studies showing dose minimization for energies that are high enough to have complete tissue penetration at 60 keV [27–30] with the added finding that the photon counting statistics will also be simultaneously maximized at this energy as

well. The K-edge of gadolinium lies within this range making it an ideal candidate for dose minimization and contrast enhancement. Other element candidates with K-edge energies that fall within the dose-optimal range that have been under recent investigation are tantalum (67 keV), ytterbium (61 keV), gold (81 keV) and bismuth (91 keV) [31]. Gadolinium is routinely used as a contrast agent for MRI-based mammography while the other metals listed do not currently have formulations approved for human use. For comparison, a molybdenum spectrum has peak energy around 17.4 keV and all the flux below 45 keV. This region has greater than an order of magnitude worse DAPT, though is one of the common anode targets used for mammography. Tungsten is a common anode target used in computed tomography. Although it has a characteristic peak around 60 keV, about 1/3 of the total flux comes from outside the optimal energy region. A LCS source, on the other hand, would have 100% of its flux within the optimal energy range.

The limitation of DAPT is that it does not consider the contrast material, nor does it quantify the attainable level of contrast. The image quality would be dependent on the relative attenuation of the contrast agent to the background, the amount of contrast agent, the size of the enhanced region, the pharmacokinetics of the contrast agent, and many other properties. This measure was designed out of a motivation to simply identify which energies would minimize the dose. Photons of energies that are 10 keV and less may deposit less energy to tissue, but such energies have only a small fraction of photons penetrating the tissue, leading to a worse DAPT. At high energies > 100 keV, most photons will pass through the object without scattering. However, when these high energy photons do interact with the medium, they tend to deposit more energy, leading to higher doses and a worse DAPT measure. Therefore, DAPT allows for the selection of energies that minimize the dose but at the same time generate images with maximized counting statistics. Making use of contrast agents found in the optimum region could yield lower noise contrast-enhanced images while simultaneously minimizing the dose.

An alternative measure would be the dose area product per contrast (DAPC). We define this similarly to DAPT, but instead consider the contrast between the enhanced ROI and the background tissue around the K-edge energy of the contrast agent.

$$DAPC \overset{\text{def}}{=} \frac{1}{2} \cdot \frac{E^{+}\left(\frac{\mu_{en}}{\rho}\right)_{b}^{+} + E^{-}\left(\frac{\mu_{en}}{\rho}\right)_{b}^{-}}{f_{x}[(\mu_{x}^{+} - \mu_{x}^{-}) - (\mu_{b}^{+} - \mu_{b}^{-})]} \tag{8}$$

Here, superscript + and − respectively represent the energy above or below the contrast element's K-edge, while subscripts x and b respectively indicate the contrast-enhanced ROI and background tissue. The mass absorption and linear attenuation coefficients are defined as before, as is the dose area product D/ϕ. In medical contexts, we typically deal with small concentrations of contrast agent relative to the surrounding tissues. In this limit, the dose area product in the numerator becomes dependent on the tissue only. The contrast in the denominator is computed from the log-attenuation of the photon counts as described in Eq. 4b for a KES image with the dependence on the effective tissue length of the contrast agent, f_x. The extra factor of ½ in front accounts for one-half of the photons used at an energy above the K-edge while the other half is used at an energy below.

The DAPC metric was computed for seven different elemental candidates using energies that are equally spaced above and below each element's K-edge. A graph that shows these DAPC calculations is presented in Figure 2(b). The DAPC was multiplied by f_x to remove the dependence on the quantity of contrast agent. Each element improves as the energies come closer to the K-edge due to the concomitant increase in contrast. Gadolinium had the smallest, and therefore best, DAPC at energies within 2% of the K-edge. The DAPC for iodine and barium is close to that of gadolinium even though their K-edge energies (33.2 keV and 37.4, respectively) are outside of the optimal DAPT range. This can be explained by the larger increase in attenuation iodine and barium have at their absorption K-edge compared to Gd. Figure 2(d) elaborates on this by plotting the relative change in the mass attenuation coefficients around the K-edge energy.

The periodic trend of increasing K-edge energy with increasing Z (see Figure 2[c]) is paired with a decreasing relative change in the mass attenuation coefficient around the element's K-edge formally known as the *jump factor* [32]. This trend is observed in Figure 2(d) and holds for energies within about 10% of the K-edge where a cross between gold and bismuth is seen. As energies further away from the K-edge are used, there comes a point where the attenuation at the above and below energies equalizes. This occurs between 27% and 30% depending on the element, beyond which the difference in attenuation becomes negative due to the lower energy attenuation being larger than the higher energy one. This point is also observed in the DAPC plot, Figure 2(b), as a discontinuity. Hence, KES improves with energies closer to the K-edge of the contrast element.

To make this general contrast agent analysis more specific to mammography, and because imparted dose is dependent on the amount of material, this analysis was repeated for a 4.2 cm thick phantom composed of a homogenous 50% fibroglandular tissue (FGT) and 50% adipose tissue. The results of the MC simulations are presented in Figure 3. The DAPT measure has a similar optimal energy range as the thin water phantom case but has a significantly worse measure for low photon energies. This is because the majority of these photons are absorbed in this size of phantom leading to a worse DAPT measure. Conventional mammography uses a molybdenum or rhodium source with peak energies in the poor DAPT region at approximately 17 keV and 20 keV, respectively. For a 4.2 cm thick breast phantom, iodine and barium now have better DAPC measures than gadolinium. This result is in agreement with a prior monoenergetic Monte Carlo study performed for iodine and gadolinium [33] and can be attributable to their larger absolute contrast $(\mu_x^+ - \mu_x^-)$ compared to gadolinium. In fact, for narrow   E around the K-edge, DAPC is ordered by atomic number for that reason. However, compared to iodine, the DAPT for gadolinium is 40% smaller while its DAPC is only 8% larger. This advantage manifests as a benefit to using gadolinium for larger phantoms and this was shown previously in the same study [33] leading to the suggestion of possibly using gadolinium for non-compressed KES mammography. This paper will continue to use a 4.2 cm phantom as is the industry standard for mammographic dose calibration.

Because Gd has acceptable DAPC with a K-edge energy within the optimal DAPT range, we choose to study Gd as the contrast agent in this paper. Moreover, in contrast to most of the other metals listed above, Gd has several FDA-approved formulations that are routinely

used in magnetic resonance imaging (MRI). This would lower the barrier for use of this contrast element if such an imaging method were to be adopted clinically. Table 2 lists some FDA-approved Gd-based contrast agents (GBCAs).

The advantage an LCS source has is that it would be tunable near the K-edge making it capable to optimize these metrics. The current bremsstrahlung-based dual-energy technologies use spectra with peak flux energies up to 40% away from the K-edge of iodine [34], making such sources less than ideal for KES imaging.

3. KES Simulation Software

Due to the computational difficulty of MC for the required fluxes to obtain a useful image at physiologically relevant concentrations of Gd, an analytic approach using Beer-Lambert (BL) attenuation was implemented using MATLAB. X-ray attenuation was calculated based on mass attenuation coefficients obtained from the National Institute of Standards and Technology (NIST) database for the gadolinium and water. Image noise was simulated using Poisson statistics as is common practice for imaging from X-ray sources [35, 36]. The phantom used was a cylindrical water phantom with a radius of 5 cm and a thickness of 4.2 cm. The thickness was chosen based on the current standard for mammography phantoms [37]. Spherical inserts with 5 and 15 mass% Gd with 2 and 3 mm radii were placed in the phantom. A graphical representation of this phantom is presented in Figure 4(a). The large concentrations of Gd were used to make the MC simulation computationally tractable requiring fewer particles to be simulated to visualize the inserts. Each simulation used 10^9 monoenergetic photons per projection at energies of 51 keV and 49 keV. The resolution of both simulations was 250 μm in each dimension. A KES image was processed, and the results are shown in Figure 5. Only photons that pass through without scattering within the phantom were used in the MC simulation to emulate the common practice of scatter filtering.

For each individual projection, the signal between the BL code and the MC simulation differs by less than 0.15% while the noise level differs by 0.69%. The KES images were produced by subtracting the intensity of the above projection from the below projection pixel-by-pixel to ensure the signal at the inserts to be greater than the background. After performing the subtraction operation, the signal of the inserts between the BL and MC KES images differed by approximately 1% in both the signal of the inserts and the noise. The BL simulation has the advantage of simulating many particles in a short amount of time. For example, simulating 10^{12} photons will take less than 0.7 CPU hours using the BL code, while the same simulation would take over 19,000 CPU hours using Monte Carlo on the same machine. Because of its clear improvement in computational difficulty, we therefore use the BL code for the remaining KES simulations in this work. A drawback of using the BL method compared to MC is the loss of scattering information. However, it is common practice to reduce scatter in projection imaging by filtering or other methods, and thus is not considered by the authors to be a limitation for this study.

4.   KES Simulations

4.1   Optimal Energy Tuning of LCS Source

The phantom used in the KES and conventional images is a cylindrical phantom similar to the one used in section 3 with a 5 cm radius and 4.2 cm depth. Instead of water, the background tissue of the phantom consisted of 11 different ratios of fibroglandular tissue and adipose tissue varying from 100% FGT to 0% FGT in 10% increments. Attenuation data for FGT and adipose tissue was taken from the International Commission on Radiation Units (ICRU) Report 44 [38]. Since cancerous breast lesions most often come from FGT with liposarcomas (cancer arising from fatty tissue) being exceedingly rare [39, 40], the spherical inserts were made with only FGT and Gd. The Gd concentrations of the inserts were adjusted to be 0.005 % and 0.015 % by mass with the aim to have physiologic accuracy to the study. These concentrations were chosen based on previous studies that estimated the concentration of a GBCA inside of various benign and malignant breast lesions, such as fibroadenoma, ductal carcinoma and lobular carcinoma, using pharmacokinetic flow models [41, 42]. The spherical symmetry of the phantom inserts was chosen due to the radial dependence on X-ray energy and flux of the LCS source as is depicted in Figure 1(c), allowing for spatial analysis of image quality if desired. The phantom used for the KES simulations is depicted in Figure 4(b).

The X-ray beam spectrum and beam profiles were simulated using a proprietary Mathematica script developed first at the Lawrence Livermore National Laboratory and optimized by Lumitron Technologies, Inc. It has been used previously to computationally characterize laser-Compton X-ray sources [11]. The script calculates the resulting Compton X-ray flux, spectrum, and spatial distribution given a simulated or experimental electron beam and laser pulse parameters. This script is based on physics and processes of laser-Compton scattering described previously [43, 44]. A 75 MeV electron beam with 1 million particles was simulated using General Particle Tracer code [45]. The phase space values of this electron beam were then modified within the Mathematica script to fit the desired beam parameters, such as electron beam energy, divergence, spot size, etc. The laser pulse is modelled as a plane wave with a Gaussian beam intensity envelope. A grid of observation angles in horizontal and vertical planes is set up. At each grid point, for each electron beam particle, the script calculates the Compton-scattered X-ray energy and the number of photons. The energy and differential cross sections of Compton-scattered X-rays are calculated using energy-momentum conservation and the Klein-Nishina formula for linearly polarized photons. The interaction probability between the electron and laser beams is calculated by integrating the photon density along the ballistic trajectory of the electron, which then multiplied by the cross-section given the number of photons within the solid angle at each grid point. Finally, contributions of all electron particles for all grid points are summed up. This Laser Compton X-ray distribution generates a 4-dimensional X-ray phase space file that can be input to our BL software employed in this paper. Computational phantoms were placed at a distance that would be completely illuminated by the X-ray beam yielding 2D projection images.

Because the integrated X-ray energy spectra can be tuned based on the electron beam energy, it is important to understand how the image quality changes with various above and below K-edge tuned X-ray energies. To maximize the contrast of the Gd inserts, the below K-edge (BKE) tuning would be ideally as close to and below the K-edge energy of Gd. For this reason, the maximum below K-edge X-ray energy $\left(E_{CE}^{B}\right)$ was tuned to be approximately 50.1 keV for all observation angles simulated. The advantage of the LCS source parameters used in this study is that they generate a divergence-limited spectrum that has a characteristic sharp drop in the maximum X-ray energy. This allows for great BKE spectrum tuning, though will not be applicable in all LCS source configurations.

Since the BKE X-ray energy tuning is fixed, the maximum above K-edge (AKE) X-ray energy $\left(E_{CE}^{A}\right)$ must be chosen to maximize image quality. This means the integrated AKE energy spectrum must have enough flux above the K-edge energy of Gd to maximize the contrast. At the same time, it should be close enough to the K-edge to take advantage of an approximately constant background signal and therefore minimize noise. However, the energy spectrum has a tailing distribution towards lower energies, therefore requiring analysis to determine the best AKE tuning to maximize image quality (see Figures 1[d] and 7[b]).

To this end, KES simulations were performed using the BL code and images were generated using 10^{14} simulated photons per projection at a pixel resolution of 500 μm × 500 μm. One projection was taken with energy tuning below the K-edge and eight others were taken above the K-edge with different energy tunings. The resulting transmission images were processed by subtracting the log of the flux adjusted AKE image from the log of the flux adjusted BKE image (see Eq. 4b) to allow for the signal at the insert to be larger than the background as is convention for medical imaging. Both methods yield very similar results, so transmission images were chosen for this study. For this analysis, the contrast-to-noise ratio (CNR) was calculated for the large inserts with 0.015% Gd according to

$$CNR = \frac{S_i - S_b}{\sqrt{\sigma_i^2 + \sigma_b^2}}.$$

(9)

Here, S_i and S_b are the mean signals of the insert and the breast phantom near the insert while σ_i and σ_b are the respected standard deviations (noise level). The background signal region was chosen to be a ring of equal area around each insert due to the spatial variation in energy and intensity of the source. The appropriate AKE energy tuning is the one where the CNR of all the inserts are simultaneously maximized. This figure of merit (FoM) was attained by normalizing the CNR curves for each insert as a function of energy, then taking the maximum of the sum curves. Mathematically, this is expressed as

$$FoM = \max_{E_{CE}^{A}} \sum_{i} \frac{CNR_i\left(E_{CE}^{A}\right)}{CNR_i(E_{\max})},$$

(10)

with i being the insert and the fraction in the sum is the CNR curve normalized so the maximum CNR equals unity. Figure 6 shows the results of the optimization simulations. The importance of this FoM is because the energy spectrum is dependent on the pixel location,

different AKE energies would result in different portions of the image having different image quality. For example, it is apparent in the CNR curves that at lower energies, the innermost inserts are favored while the outermost inserts have a lower image quality. This is because the average energy from an LCS source is radially dependent with higher energies in the middle and lower energies at the periphery (see Figures 1[c] and 6[d]). The FoM defined above appropriately chooses the energy in which the image quality is maximized globally over the phantom, as can be seen with the corresponding peaks in Figure 6.

The best $\left(E_{CE}^{A}\right)$ tunings to perform KES simulations were found to be approximately 50.7 keV, 50.8 keV, 51 keV, 52 keV, and 53.5 keV for the 0.5%, 1%, 2%, 6%, and 11% bandwidths, respectively. These energy tunings will be used for the remaining KES simulations in this study. Generally, the CNR is dependent on the insert location. For example, from the results, insert pairs 1/7, 2/8, and 3/9 have similar CNRs, especially at larger bandwidths. Since these inserts are at similar radial distances from the center of the phantom, they are subject to the same energies from the LCS X-ray spectrum. However, the inserts in this phantom are embedded in background tissue of varying composition of fibroglandular and adipose tissue. Since the inserts 1, 2 and 3 are in an environment with a higher fraction of FGT, the CNRs of these inserts are lower than those of similar size and concentrations lying in a lower FGT density region. Due to the characteristic dipole radiation pattern of the LCS spectrum (see Figure 1), there is more photon flux in the vertical dimension compared to the horizontal dimension. In a scenario where the density of the background tissue was more homogeneous, it is expected that the more equatorially aligned inserts 1, 2, and 3 would have a slightly smaller CNR than their more vertically aligned counterparts (inserts 7, 8 and 9). We also performed this computational experiment and only a minimal difference in CNR was observed. LCS spectra that have more spatial variance in flux would likely be more sensitive to this phenomenon.

At larger bandwidths, the CNR becomes negative for some inserts at some AKE energies. This happens at AKE energies that do not provide enough flux of photons near the K-edge energy of Gd, like the inserts that are far from the center of the phantom as can be seen in Figure 6(c). Combined with the low physiologic concentration of Gd, the attenuation of the insert that is primarily composed of FGT to represent a glandular tumor ends up larger than the surrounding tissue that is composed of some adipose tissue. The result is a signal that is lower at the insert, and therefore has a negative CNR. It is important to note that most imaging studies report the absolute value of the CNR. Here, we allow the possibility of negative CNR as it provides important conceptual information as described above and highlights the benefits of the narrow bandwidths that are achievable using LCS sources.

Figure 6(d) shows how the mean energy contours change with increasing electron beam energy. CNR is maximized when this energy is just high enough to have the K-edge energy contour encompassing all the inserts. Increasing the electron beam energy from this point decreases image quality as the X-ray attenuation of Gd falls with increasing energy. Therefore, in future implementation of LCS KES imaging, the object should be placed at a distance such that mean energy contour for the Gd K-edge in the AKE spectrum just reaches the edge of the imaging region of interest for the best possible contrast.

4.2   LCS KES Imaging Compared to Conventional Imaging from a Bremsstrahlung Source

It is of primary interest of this paper to compare how the dose and image quality of LCS compares to that of the current industry standard bremsstrahlung source. To this end, we apply the same BL code to create an absorption image on the same phantom using a 25 kVp molybdenum (Mo) spectrum with a 0.03 mm Mo filter. A Mo source, along with Rh, is a common source used for screening mammograms due to a large peak around 17.4 keV for Mo and 20 keV for Rh, which happens to be around the energy where breast and adipose tissue absorb the most dose allowing for the best quality absorption image [27]. Approximately 99.5% of the photons are absorbed or scattered at the energy with peak flux from a Mo source. Such a characteristic is useful for absorption images but is non-beneficial in KES and to the patient due to maximum dose-deposition. The spectrum used was generated using the SpekPy v2.0 Python toolkit [46] and is shown in Figure 7 along with a comparison of the 2% bandwidth LCS AKE and BKE spectra.

KES images were generated at varying bandwidths (0.5%, 1%, 2%, 6% and 11%) and total number of photons per projection ($10^{12} - 10^{14}$ ph/projection). Each KES simulation was generated using $\left(E_{CE}^{B}\right) = 50.1$ keV for the BKE image and the corresponding best $\left(E_{CE}^{A}\right)$ found for the AKE image. To keep the number of particles constant across all computational experiments, Mo simulations were run for twice the number of photons per projection as a conventional absorption image only uses one projection while a KES image requires two. As conventional X-rays are generated by depositing high energy electrons on a target resulting in bremsstrahlung radiation, the radiation pattern is broad and material dependent. LCS in comparison has a much narrower energy spectrum that can be tuned to the desired energies, such as above and below the K-edge of contrast material.

The images resulting from the KES and conventional simulations for the 10^{12}, 10^{13}, and 10^{14} ph/projection cases are presented in Figure 8. Figure 8(a) shows the raw images without post-processing. These are the images used for later analysis. While Figure 8(b) shows the images after applying a threshold to the upper and lower signal bounds. These thresholds were arbitrarily chosen so that all densities and enhancements within the phantom can be distinguished simultaneously as best as possible. Application of a threshold is a common practice performed to resolve structures in radiographic imaging. The similarity between all fluxes of the conventional bremsstrahlung simulations is due to the lower noise associated with a single image as opposed to a composition of two images that KES uses.

Figure 9 shows in more detail the qualitative effects of the thresholds using the 0.5% BW case at 10^{14} ph/projection. The color of the area outside of the phantom was set to black in these images to help visualize the thresholds better with a contrasting background. The upper and lower signal bounds can be adjusted to highlight areas of the phantom that require a more isolated interpretation. As the lower bound is increased, the distracting breast tissue starts to disappear. Such a threshold would be useful in the scenario of overlaying a KES image with an absorption image to retain useful anatomical information while also highlighting the areas of suspicion found in the KES image. As the upper bound is decreased, the inserts among the higher density backdrop become more pronounced. The variation in the background also becomes apparent while adjusting this threshold. There

is both a linear sloping due to the regular variation in fibroglandular tissue density in the phantom by construction as well as a rounded contour to the background that is due to the radial dependence on the X-ray energy from the LCS source. These background artifacts could be accommodated for using more complicated post-processing measures if desired. Adjusting both the upper and lower bounds simultaneously would also allow for a more isolated insert enhancement if desired.

In general, the smaller the bandwidth of the LCS spectra used will improve the quality of the image with the 0.5% BW simulation creating the best subtraction image. This can be attributed to a higher fraction of photons being above and closer to the K-edge energy at smaller bandwidths. The lower concentration inserts with 3 mm radius can be seen only slightly in the lower flux images that have BW 2% or less and are not discernable in the low-flux 6% BW image. Thresholding of the higher flux images makes the low concentration inserts more easily visible for the large bandwidth simulations. Resampling of the to a lower resolution could also help resolve these structures if needed.

In the 25 kVp Mo-Mo simulation, it is easier to see the inserts as the fraction of glandular tissue drops. In the regions with high fractions of FGT, the inserts are no longer visible for the conventional simulation due to the highly similar attenuation with the background. The conventional simulations also show the vertical striations due to the variation in breast tissue density. In the KES simulations, the background is subtracted away, so this feature is less pronounced. Though the background can still be resolved in the KES images, especially in the higher BW simulations as well as the high-flux images with thresholds applied (see Figure 8).

In a clinical context, the disappearing inserts in high FGT regions is the difficulty of screening mammography for patients with dense breasts, as such lesions would "hide" within the attenuating dense fibroglandular backdrop. With regards to the inserts that are easily seen in the low FGT regions, these structures may or may not be suspicious for cancerous lesions, only that they have a different density relative to its neighborhood. Furthermore, all inserts in the conventional simulation have the same level of attenuation no matter how much Gd is present (see Figure 8[b]). This is a direct consequence of the low Gd concentrations present in the inserts and would not be true otherwise. So, the advantage of KES is that it can specifically identify regions that are enhancing with contrast material as well as quantify the amount of the uptake given by the intensity of the signal. This feature is particularly useful, since it is known that cancerous lesions, in general, uptake contrast in greater amounts and at greater velocity than benign lesions [41, 42, 47–49]. Hence, discrimination can be made between cancerous and benign lesions by both timing and signal intensity on the KES image, which would not be possible using a conventional source at the low concentrations of Gd. This difference in contrast can be seen in any of the KES images in Figures 8 and 9.

To obtain an estimate of the mean glandular dose (MGD) imparted to the phantom, we employ the following formula that was derived from first principles by Boone [27]:

$$MGD = \frac{A}{m_g} \sum_E E f(E) \phi(E) G(E).$$

(11)

Eq. (11) is similar to the dose relation used for DAPC but has the difference that it accounts for the dose imparted only to the fibroglandular tissue present in the phantom. A is the cross-sectional area of the phantom, m_g is the mass of the glandular tissue in the phantom, E is the photon energy, and ϕ is the fluence of incoming photons per area as a function of energy. G is the adjustment for the energy deposited into glandular tissue only and is defined as

$$G = \frac{f_g \left(\frac{\mu_{en}}{\rho}\right)_g}{f_g \left(\frac{\mu_{en}}{\rho}\right)_g + (1 - f_g)\left(\frac{\mu_{en}}{\rho}\right)_a},$$

(12)

with the subscripts a and g to represent adipose and fibroglandular tissue and f_g is the fraction of FGT. Finally, $f(E)$ is the fractional energy deposited by the photon described as the amount of energy deposited divided by the energy of the photon. The values for f were taken from Boone and linearly interpolated to an overall 50% glandular phantom with 4.2 cm thickness.

Applying the above formula gives an approximate dose per photon for each image that can be scaled to the number of photons that is used in the respective simulation. The calculated MGD for each source is listed in Table 3. It is observed that the dose increases as the bandwidth increases. This can be attributed to the increase in flux of lower energy photons that deposit more dose into the phantom. The largest relative dose was that using the conventional 25 kVp Mo-Mo X-ray spectrum as is expected since most of the flux from the Mo-Mo spectrum is near the peak of fractional energy deposition curve for breast tissue [27]. Unexpectedly, the MGD from a conventional source is not much higher than that from the LCS KES protocol. Although photons of energies from a 25 kVp Mo source deposit a higher fraction of their energy, the energy is low enough so that the total energy deposited is not much different in comparison to the photon energies used for LCS KES. For example, approximating the fractional energy depositions for 20 keV and 50 keV photons, $f(20) \approx$ 0.5, $G(20) \approx 0.57$, $f(50) \approx 0.13$ and $G(50) \approx 0.54$ for a 4.2 cm thick phantom with 50% homogeneous glandularity. This means a 20 keV photon would deposit about 5.7 keV into glandular tissue while a 50 keV photon would deposit a smaller, yet comparable, 3.5 keV into glandular tissue.

Both CNR and relative contrast ratio (RCR) were employed to quantify the image quality of each insert. RCR is described as

$$RCR = \left| \frac{S_i - S_b}{S_b} \right|.$$

(13)

Ratios of each contrast metric and dose were compared between LCS KES and conventional images. The ratio of RCR and dose (RCRD) compared to conventional (CONV) images is defined to be

$$RCRD = \frac{RCR_{LCS}/Dose_{LCS}}{RCR_{CONV}/Dose_{CONV}}. \qquad (14)$$

This metric can be interpreted as the ratio of contrast normalized to dose. The inverse metric, dose reduction normalized to contrast (DRCR), is also of use and is simply the inverse of RCRD. A similar metric based on CNR is also used for analysis of image quality and dose defined as

$$CNRD = \frac{CNR_{LCS}/Dose_{LCS}}{CNR_{CONV}/Dose_{CONV}}, \qquad (15)$$

which has a similar interpretation as the above metric with inverse being the dose reduction normalized to contrast-to-noise (DCNR).

The results from the analysis using the above metrics are presented in Table 4 for the 10^{12} and 10^{14} photon simulations. Inserts were grouped into four categories due to their similar contrast metric values in the LCS KES simulations and averaged together. The inserts were classified as follows: high contrast large radius (HCLR) – inserts 1, 2, 3, 7, 8 and 9; high contrast small radius (HCSR) – inserts 4, 5, 6, 10, 11 and 12; low contrast large radius (LCLR) – inserts 13, 14, 15, 19, 20 and 21; low contrast small radius (LCSR) – inserts 16, 17, 18, 22, 23 and 24.

As was observed qualitatively in the KES images above, the contrast at the insert relative to the background tissue increases with increasing Gd concentration and insert size. The increase is expected and based on the quantity of the materials within rather than on the flux. Constant relative contrast is also observed across fluxes where the 10^{12} ph/projection has the same RCR to an image generated with 10^{14} ph/projection for every insert. This constancy across different values of flux is due to the normalization of the images for flux. The RCR is also the same across the bremsstrahlung simulations for the same reason. However, the RCR is not as predictable since the signal is not predominantly dependent on Gd concentrations, as with the KES simulations, but instead is predominantly dependent on the tissue density. This led to a higher average RCR for the LCLR compared to the HCLR group. The metric that is dependent on the flux is CNR, which generally increases with increasing flux due to the reduction in noise. This trend is observed in the data. The CNR is generally higher at the larger concentrations and insert radii for the LCS KES simulations. This is not the case for the Mo simulation as the image quality of the inserts is dependent on the local densities which can be highly variable. The trend in CNR is retained for the LCS KES simulations as the background tissue is subtracted out of the image and the signal becomes predominantly dependent on the amount of Gd only.

For the 25 kVp bremsstrahlung simulations, the CNR increases only minimally when increasing the total number of photons. This is a consequence of the phantom choice. As spheres were used for the insert objects, this creates a radial dependence on the path length. This in turn creates a variation in the signal that scales as N (number of photons) for large N. Since Poisson noise goes like $\sqrt{N}$, the added variation overcomes the Poisson noise resulting

in a CNR that becomes approximately constant for large numbers of photons. If cylindrical inserts were chosen, the CNR would scale according to the Poisson noise.

The RCRs for the LCS KES images are greater at every 0.015% Gd insert compared to the conventional image, showing the advantage of using the K-edge of Gd for contrast enhancement. The lower concentrations inserts have lower RCR compared to the conventional image for BWs of 6% and above. As for CNR, the conventional source does better at low fluxes, such as 2×10^{12} total photons per image as seen in the table. For larger fluxes $> 10^{13}$ ph/projection, the CNR for the LCS KES simulations then outperforms that of the bremsstrahlung source at the same flux. At lower fluxes, it is likely the added noise from the subtraction of two images is what gives the KES simulation lower CNRs compared to conventional which only uses one image.

Comparing the LCS KES simulations to the Mo simulations, there is up to a 29x increase in relative contrast normalized to dose in the 2×10^{12} ph/image simulations. Looking at the inverse metric (DRCR), this would indicate that an image at the same relative contrast can be obtained at only 3% of the dose. Considering the 14% decrease in MGD per photon in the 0.5% BW LCS simulation compared to the conventional one, this benefit largely comes from the 25 times increase in relative contrast that KES provides. The CNRD at this same flux, however, showed no improvement compared to the bremsstrahlung simulation.

When increasing the flux to 2×10^{14} ph/image, the dose normalized CNR of the LCS KES simulation improves over the conventional image by 4 times for the smallest bandwidth simulation. From the inverse DCNR perspective, the same quality image as a 25 kVp Mo-Mo source can be obtained using a 0.5% BW LCS source at only one-quarter of the dose. Of course, this image quality falls by increasing the bandwidth as more of the flux has energies that are further away from the K-edge. This is seen in Table 4 with the 6% BW KES simulation having a maximum averaged CNRD of 1.72 compared to the 0.5% BW maximum of 4.05 or the 2% BW maximum of 3.27.

5. Conclusion

This paper explored the use of LCS in CEDM and other KES imaging using Gd as the contrast agent. Gd has been proposed before to decrease dose and as an alternative to patients with known drug allergies to iodinated contrast agents or renal insufficiency [50, 51]. The use of Gd for LCS KES imaging has also been proposed [8, 9], but never investigated thoroughly until now. It was found that, when normalized for dose, there was marked increase in contrast up to 29x compared to a conventional 25 kVp Mo-Mo bremsstrahlung source. Conversely, this corresponds to a 97% dose decrease to attain the same level of relative contrast. There was also a flux and BW-dependent increase in dose-normalized CNR for the LCS source up to 4x for a flux of 10^{14} ph/projection.

However, at such fluxes, the dose may be prohibitive for a screening study. For example, the 0.5% BW LCS spectra used in this study had an estimated MGD of 3.56×10^{-15} Gy ph^{-1}. This corresponds to a MGD of 3.56 mGy for a study that employs 10^{12} ph/projection, which is already 0.56 mGy above what the American College of Radiology recommends for

a 4.2 cm depth phantom [37]. At this flux, there was no improvement in CNRD even at the highest concentration of Gd studied. Before making a conclusion regarding how beneficial such a study would be, the imaging modality must be considered. In a KES image, the background is subtracted away leaving only the tissue that has undergone significant Gd uptake. In a conventional image, all tissue remains, leaving the possibility of suspicious lesions being obscured by dense fibroglandular tissue, and at the low Gd concentrations, there is no way to distinguish an enhanced lesion from non-enhancing tissue based on attenuation alone. Even though the CNR for LCS KES is low compared to conventional at a flux of 10^{12} ph/projection, there may still be clinical merit to using it as a screening modality due to the large difference in relative contrast between the Gd enhanced region and the background. In a less-frequent diagnostic scenario, a higher flux study may be appropriate. It is possible to mitigate the dose by cutting off the source once a minimum contrast requirement has been met. Although, this would only be effective at decreasing the dose in those with a positive screening test.

The low concentrations of Gd inside of breast lesions is the largest limiting factor for the dose. This limitation may be overcome in a number of ways. Considering GBCAs have excellent renal clearance and the median lethal dose of GBCAs (8 mmol kg^{-1} for Gd-DTPA and > 30 mmol kg^{-1} for gadodiamide [52, 53]) is significantly higher than the clinically used dose of 0.1 mmol kg^{-1}, using higher doses for KES imaging might be a possibility. Alternatively, the Gd concentration in breast lesions may be increased by coming up with a chelating agent that shows higher uptake or specific affinity for these lesions, or by choosing another agent that has larger uptake. For instance, iodinated contrast agents have been estimated to have up to 10x greater uptake in breast lesions compared to GBCAs [54]. Such a concentration of iodine would lead to a near 10x lower DAPC metric and therefore theoretically be able to obtain an image with an order of magnitude fewer photons. This was in fact done in a previous computational study where the authors were able to obtain a KES image with 5×10^{10} photons at 0.3×0.3 mm^2 resolution and the estimated dose was smaller by almost an order of magnitude [55]. In the case of larger path lengths, gadolinium has been shown to make images of equal contrast with lower dose compared to iodine [33]. This would enable compression free dual energy mammography using gadolinium-based contrast agents.

Because the sensitivity of CEDM has been shown to be comparable to Gd contrast-based MRI [3], it may be possible to offer LCS KES imaging as an alternative. An MRI study takes between 20 minutes to over an hour, while the source parameters examined in this paper would be able to take an image within seconds of exposure at the resulting fluxes. Considering the source studied in this paper requires two energy tunings, the rate-limiting step for overall imaging time is the energy switching process. This could be on the order of minutes yet is still significantly faster than MRI. Moreover, the spatial resolution of a clinical MRI is typically on the order of 1 mm and can be as large as 5 mm in the scanning dimension. This paper showed that a resolution of 250 μm is viable under the studied conditions. Therefore, it is conceivable that LCS KES can be a much faster and better resolved alternative to MRI. Moreover, while this paper used a relatively large detector area to have the entire phantom in the field of view, the ultimate resolution obtainable from a

laser-Compton source will be related to the photon-electron interaction spot size which, for next generation sources, is on the order of 5 microns.

Acknowledgments.

Data availability.

Data underlying the results presented in this paper are not publicly available at this time but may be obtained from the authors upon reasonable request.

References

1. Weigel S, Heindel W, Heidrich J, Hense HW, and Heidinger O, "Digital mammography screening: sensitivity of the programme dependent on breast density," Eur Radiol 27, 2744–2751 (2017). [PubMed: 27822617]

2. Yaffe MJ and Mainprize JG, "Risk of Radiation-induced Breast Cancer from Mammographic Screening," Radiology 258, 98–105 (2011). [PubMed: 21081671]

3. Jochelson MS, Dershaw DD, Sung JS, Heerdt AS, Thornton C, Moskowitz CS, Ferrara J, and Morris EA, "Bilateral contrast-enhanced dual-energy digital mammography: feasibility and comparison with conventional digital mammography and MR imaging in women with known breast carcinoma," Radiology 266, 743–751 (2013). [PubMed: 23220903]

4. Kulpe S, Dierolf M, Günther B, Brantl J, Busse M, Achterhold K, Pfeiffer F, and Pfeiffer D, "Spectroscopic imaging at compact inverse Compton X-ray sources," Physica Medica 79, 137–144 (2020). [PubMed: 33271418]

5. Thomlinson W, Elleaume H, Porra L, and Suortti P, "K-edge subtraction synchrotron X-ray imaging in bio-medical research," Physica Medica 49, 58–76 (2018). [PubMed: 29866345]

6. Stevenson AW, Crosbie JC, Hall CJ, Hausermann D, Livingstone J, and Lye JE, "Quantitative characterization of the X-ray beam at the Australian Synchrotron Imaging and Medical Beamline (IMBL)," Journal of Synchrotron Radiation 24, 110–141 (2017). [PubMed: 28009552]

7. Zhao Y, Brun E, Coan P, Huang Z, Sztrokay A, Diemoz PC, Liebhardt S, Mittone A, Gasilov S, Miao J, and Bravin A, "High-resolution, low-dose phase contrast X-ray tomography for 3D diagnosis of human breast cancers," Proc Natl Acad Sci U S A 109, 18290–18294 (2012). [PubMed: 23091003]

8. Kulpe S, Dierolf M, Braig E, Günther B, Achterhold K, Gleich B, Herzen J, Rummeny E, Pfeiffer F, and Pfeiffer D, "K-edge subtraction imaging for coronary angiography with a compact synchrotron X-ray source," PLOS ONE 13, e0208446 (2018). [PubMed: 30532277]

9. Kulpe S, Dierolf M, Braig EM, Günther B, Achterhold K, Gleich B, Herzen J, Rummeny E, Pfeiffer F, and Pfeiffer D, "K-edge subtraction imaging for iodine and calcium separation at a compact synchrotron x-ray source," J Med Imaging (Bellingham) 7, 023504 (2020). [PubMed: 32341936]

10. Albert F, Anderson SG, Gibson DJ, Hagmann CA, Johnson MS, Messerly M, Semenov V, Shverdin MY, Rusnak B, Tremaine AM, Hartemann FV, Siders CW, McNabb DP, and Barty CPJ, "Characterization and applications of a tunable, laser-based, MeV-class Compton-scattering $\ensuremath{\gamma}$-ray source," Physical Review Special Topics - Accelerators and Beams 13, 070704 (2010).

11. Hwang Y, "Characterization and Applications of Laser-Compton X-Ray Source," Ph.D. (University of California, Irvine, Ann Arbor, 2018).

12. Habs D, Tajima T, and Zamfir V, "Extreme Light Infrastructure–Nuclear Physics (ELI–NP): New Horizons for Photon Physics in Europe," Nuclear Physics News 21, 23–29 (2011).

13. Anderson SG, Albert F, Bayramian AJ, Beer G, Bonanno RE, Cross RR, Deis G, Ebbers CA, Gibson DJ, Hartemann FV, Houck TL, Marsh RA, McNabb DP, Messerly MJ, Scarpetti RD, Shverdin MY, Siders CW, Wu SS, Barty CPJ, Adolphsen CE, Chu TS, Jongewaard EN, Li Z, Limborg C, Tantawi SG, Vlieks AE, Wang F, Wang JW, Zhou F, and Raubenheimer TO, "VELOCIRAPTOR: An X-band photoinjector and linear accelerator for the production of Mono-Energetic γ-rays," Nuclear Instruments and Methods in Physics Research A 657, 140 (2011).

14. Sun C and Wu YK, "Theoretical and simulation studies of characteristics of a Compton light source," Physical Review Special Topics - Accelerators and Beams 14, 044701 (2011).

15. Hartemann FV, Brown WJ, Gibson DJ, Anderson SG, Tremaine AM, Springer PT, Wootton AJ, Hartouni EP, and Barty CPJ, "High-energy scaling of Compton scattering light sources," Physical Review Special Topics - Accelerators and Beams 8, 100702 (2005).

16. Bhatt G, Grotch H, Kazes E, and Owen DA, "Relativistic spin-dependent Compton scattering from electrons," Physical Review A 28, 2195–2200 (1983).

17. Engström A, "Quantitative micro- and histochemical elementary analysis by roentgen absorption spectrography," Acta radiol. (1946).

18. Engström A, "Note on the Cytochemical Analysis of Elements by Roentgen Rays," Acta Radiologica os-36, 393–396 (1951).

19. Jacobson B, "Dichromatic Absorption Radiography. Dichromography," Acta Radiologica os-39, 437–452 (1953).

20. Clark GL, "Medical, biological and industrial applications of monochromatic radiography and microradiography," Radiology 49, 483–495 (1947). [PubMed: 20267899]

21. Francescone MA, Jochelson MS, Dershaw DD, Sung JS, Hughes MC, Zheng J, Moskowitz C, and Morris EA, "Low energy mammogram obtained in contrast-enhanced digital mammography (CEDM) is comparable to routine full-field digital mammography (FFDM)," European Journal of Radiology 83, 1350–1355 (2014). [PubMed: 24932846]

22. James JJ and Tennant SL, "Contrast-enhanced spectral mammography (CESM)," Clinical Radiology 73, 715–723 (2018). [PubMed: 29937340]

23. Luczy ska E, Heinze-Paluchowska S, Dyczek S, Blecharz P, Rys J, and Reinfuss M, "Contrast-enhanced spectral mammography: comparison with conventional mammography and histopathology in 152 women," Korean J Radiol 15, 689–696 (2014). [PubMed: 25469079]

24. Schlegel W and Bille J, Medizinische Physik 2 (Springer Verlag, Berlin, Heidelberg, 1999).

25. Perl J, Shin J, Schumann J, Faddegon B, and Paganetti H, "TOPAS: an innovative proton Monte Carlo platform for research and clinical applications," Med Phys 39, 6818–6837 (2012). [PubMed: 23127075]

26. Allison J, Amako K, Apostolakis J, Arce P, Asai M, Aso T, Bagli E, Bagulya A, Banerjee S, Barrand G, Beck BR, Bogdanov AG, Brandt D, Brown JMC, Burkhardt H, Canal P, Cano-Ott D, Chauvie S, Cho K, Cirrone GAP, Cooperman G, Cortés-Giraldo MA, Cosmo G, Cuttone G, Depaola G, Desorgher L, Dong X, Dotti A, Elvira VD, Folger G, Francis Z, Galoyan A, Garnier L, Gayer M, Genser KL, Grichine VM, Guatelli S, Guèye P, Gumplinger P, Howard AS, H ivná ová I, Hwang S, Incerti S, Ivanchenko A, Ivanchenko VN, Jones FW, Jun SY, Kaitaniemi P, Karakatsanis N, Karamitros M, Kelsey M, Kimura A, Koi T, Kurashige H, Lechner A, Lee SB, Longo F, Maire M, Mancusi D, Mantero A, Mendoza E, Morgan B, Murakami K, Nikitina T, Pandola L, Paprocki P, Perl J, Petrovi I, Pia MG, Pokorski W, Quesada JM, Raine M, Reis MA, Ribon A, Risti Fira A, Romano F, Russo G, Santin G, Sasaki T, Sawkey D, Shin JI, Strakovsky II, Taborda A, Tanaka S, Tomé B, Toshito T, Tran HN, Truscott PR, Urban L, Uzhinsky V, Verbeke JM, Verderi M, Wendt BL, Wenzel H, Wright DH, Wright DM, Yamashita T, Yarba J, and Yoshida H, "Recent developments in Geant4," Nuclear Instruments and Methods in Physics Research Section A: Accelerators, Spectrometers, Detectors and Associated Equipment 835, 186–225 (2016).

27. Boone JM, "Glandular Breast Dose for Monoenergetic and High-Energy X-ray Beams: Monte Carlo Assessment," Radiology 213, 23–37 (1999). [PubMed: 10540637]

28. Luxton G and Jozsef G, "Radial dose distribution, dose to water and dose rate constant for monoenergetic photon point sources from 10 keV to 2 MeV: EGS4 Monte Carlo model calculation," Medical physics 26, 2531–2538 (1999). [PubMed: 10619236]

29. Zankl PN, Fehrenbacher G, and Drexler G, "Dose distributions in the ICRU sphere for monoenergetic photons and electrons and for ca. 800 radionuclides," (GSF-Bericht, 1993).

30. Rogers DW, "Notes on the structure of radiotherapy depth-dose distributions," CLRP Report CLRP 07 01, Carleton Laboratory for Radiotherapy Physics Physics Department, Carleton University, Ottawa, Canada (2009).

31. FitzGerald PF, Colborn RE, Edic PM, Lambert JW, Torres AS, Bonitatibus J. Peter J., and Yeh BM, "CT Image Contrast of High-Z Elements: Phantom Imaging Studies and Clinical Implications," Radiology 278, 723–733 (2016). [PubMed: 26356064]

32. Armstrong JT, "Quantitative analysis of silicate and oxide materials : comparison of monte carlo, ZAF, and $\psi(\rho z)$ procedures," Microbeam Analysis, 239–246 (1988).

33. Sarnelli A, Elleaume H, Taibi A, Gambaccini M, and Bravin A, "K-edge digital subtraction imaging with dichromatic x-ray sources: SNR and dose studies," Physics in Medicine and Biology 51, 4311–4328 (2006). [PubMed: 16912383]

34. Puong S, Bouchevreau X, Patoureaux F, Iordache R, and Muller S, Dual-energy contrast enhanced digital mammography using a new approach for breast tissue canceling, Medical Imaging (SPIE, 2007), Vol. 6510.

35. Prince JL and Links JM, Medical imaging signals and systems (Pearson Prentice Hall Upper Saddle River, 2006).

36. Macovski A, Medical imaging systems (Prentice Hall, 1983).

37. Berns EA, "2018 Digital Mammography Quality Control Manual," A. C. o. Radiology, ed. (2020).

38. White DR, Booz J, Griffith RV, Spokas JJ, and Wilson IJ, "Report 44," Journal of the International Commission on Radiation Units and Measurements os23, NP-NP (2016).

39. Kennedy T and Biggart JD, "Sarcoma of the breast," Br J Cancer 21, 635–644 (1967). [PubMed: 4294611]

40. McGowan TS, Cummings BJ, O'Sullivan B, Catton CN, Miller N, and Panzarella T, "An analysis of 78 breast sarcoma patients without distant metastases at presentation," International Journal of Radiation Oncology*Biology*Physics 46, 383–390 (2000). [PubMed: 10661345]

41. Brix G, Kiessling F, Lucht R, Darai S, Wasser K, Delorme S, and Griebel J, "Microcirculation and microvasculature in breast tumors: Pharmacokinetic analysis of dynamic MR image series," Magnetic Resonance in Medicine 52, 420–429 (2004). [PubMed: 15282828]

42. Renz DM, Diekmann F, Schmitzberger FF, Pietsch H, Fallenberg EM, Durmus T, Huppertz A, Böttcher J, Bick U, Hamm B, and Lawaczeck R, "Pharmacokinetic Approach for Dynamic Breast MRI to Indicate Signal Intensity Time Curves of Benign and Malignant Lesions by Using the Tumor Flow Residence Time," Investigative Radiology 48, 69–78 (2013). [PubMed: 23262793]

43. Terrall JR, "Elementary Treatment of Relativistic Cross Sections," American Journal of Physics 38, 1460–1474 (1970).

44. Wang J and Huang W-H, "Spectral distributions of the scattered photons within an acceptance angle in Thomson scattering," Chinese Physics C 35, 203–208 (2011).

45. De Loos M and Van Der Geer S, "General Particle Tracer: A new 3D code for accelerator and beamline design," in 5th European Particle Accelerator Conference, 1996), 1241.

46. Poludniowski G, Omar A, Bujila R, and Andreo P, "Technical Note: SpekPy v2.0—a software toolkit for modeling x-ray tube spectra," Medical Physics 48, 3630–3637 (2021). [PubMed: 33993511]

47. Kaiser WA and Zeitler E, "MR imaging of the breast: fast imaging sequences with and without Gd-DTPA. Preliminary observations," Radiology 170, 681–686 (1989). [PubMed: 2916021]

48. Malich A, Fischer DR, Wurdinger S, Boettcher J, Marx C, Facius M, and Kaiser WA, "Potential MRI Interpretation Model: Differentiation of Benign from Malignant Breast Masses," American Journal of Roentgenology 185, 964–970 (2005). [PubMed: 16177416]

49. Huang W, Tudorica LA, Li X, Thakur SB, Chen Y, Morris EA, Tagge IJ, Korenblit ME, Rooney WD, Koutcher JA, and Charles J Springer S, "Discrimination of Benign and Malignant Breast

Lesions by Using Shutter-Speed Dynamic Contrast-enhanced MR Imaging," Radiology 261, 394–403 (2011). [PubMed: 21828189]

50. Sam AD, Morasch MD, Collins J, Song G, Chen R, and Pereles FS, "Safety of gadolinium contrast angiography in patients with chronic renal insufficiency," Journal of Vascular Surgery 38, 313–318 (2003). [PubMed: 12891113]

51. Sayin T, Turhan S, Akyürek Ö, and Kilickap M, "Gadolinium:Nonionic Contrast Media (1:1) Coronary Angiography in Patients With Impaired Renal Function," Angiology 58, 561–564 (2007). [PubMed: 17906283]

52. Gries H, "Extracellular MRI Contrast Agents Based on Gadolinium," in Contrast Agents I: Magnetic Resonance Imaging, Krause W, ed. (Springer Berlin Heidelberg, Berlin, Heidelberg, 2002), pp. 1–24.

53. Kaplan GD, Aisen AM, and Aravapalli SR, "Preliminary clinical trial of gadodiamide injection: A new nonionic gadolinium contrast agent for MR imaging," Journal of Magnetic Resonance Imaging 1, 57–62 (1991). [PubMed: 1802131]

54. Jong RA, Yaffe MJ, Skarpathiotakis M, Shumak RS, Danjoux NM, Gunesekara A, and Plewes DB, "Contrast-enhanced Digital Mammography: Initial Clinical Experience," Radiology 228, 842–850 (2003). [PubMed: 12881585]

55. Paternò G, Cardarelli P, Gambaccini M, and Taibi A, "Dual-Energy X-ray Medical Imaging with Inverse Compton Sources: A Simulation Study," Crystals 10, 834 (2020).
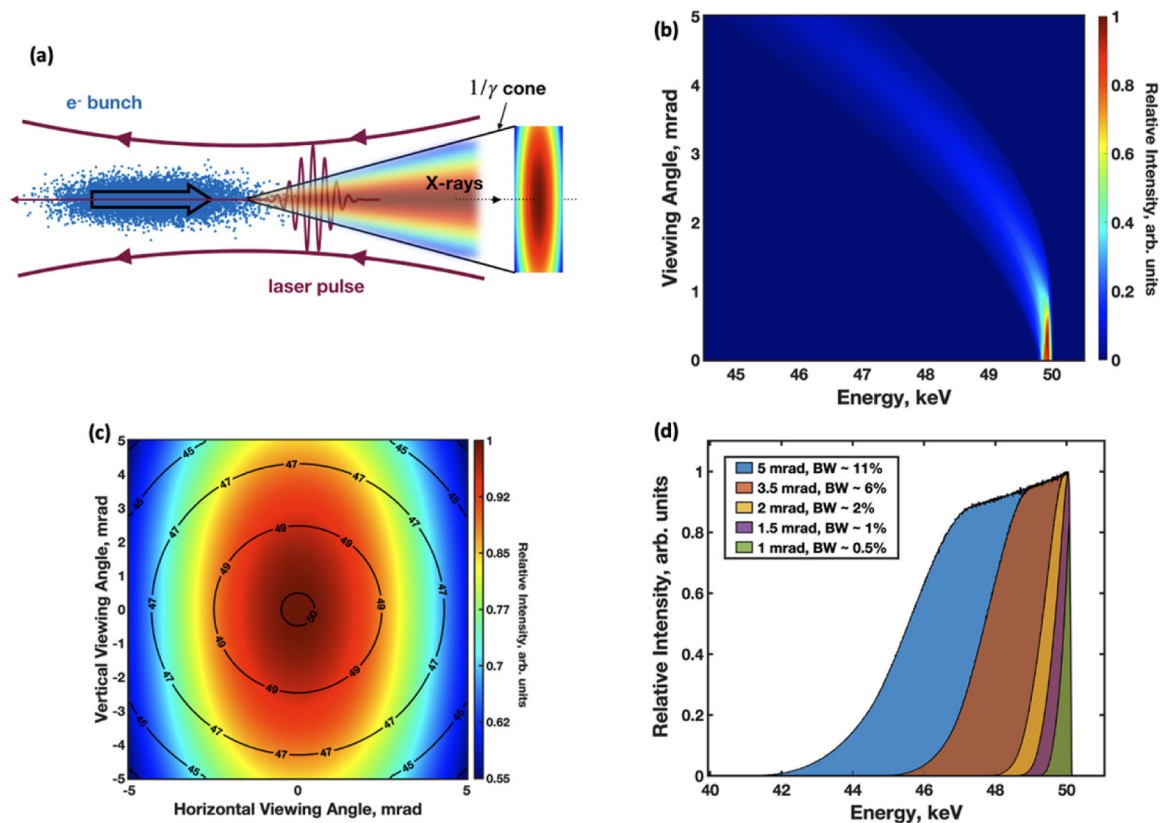
Fig. 1.
Energy spectra of the LCS source tuned to CE energy of 50.1 keV: (a) schematic of the electron bunch and laser beam interaction in LCS, (b) energy and intensity as a function of viewing angle, (c) spatial intensity cross section with overlayed mean energy contours for a 5 mrad aperture, (d) integrated energy spectra with varying aperture sizes. The bandwidths (BW) provided were calculated using E/E at FWHM.
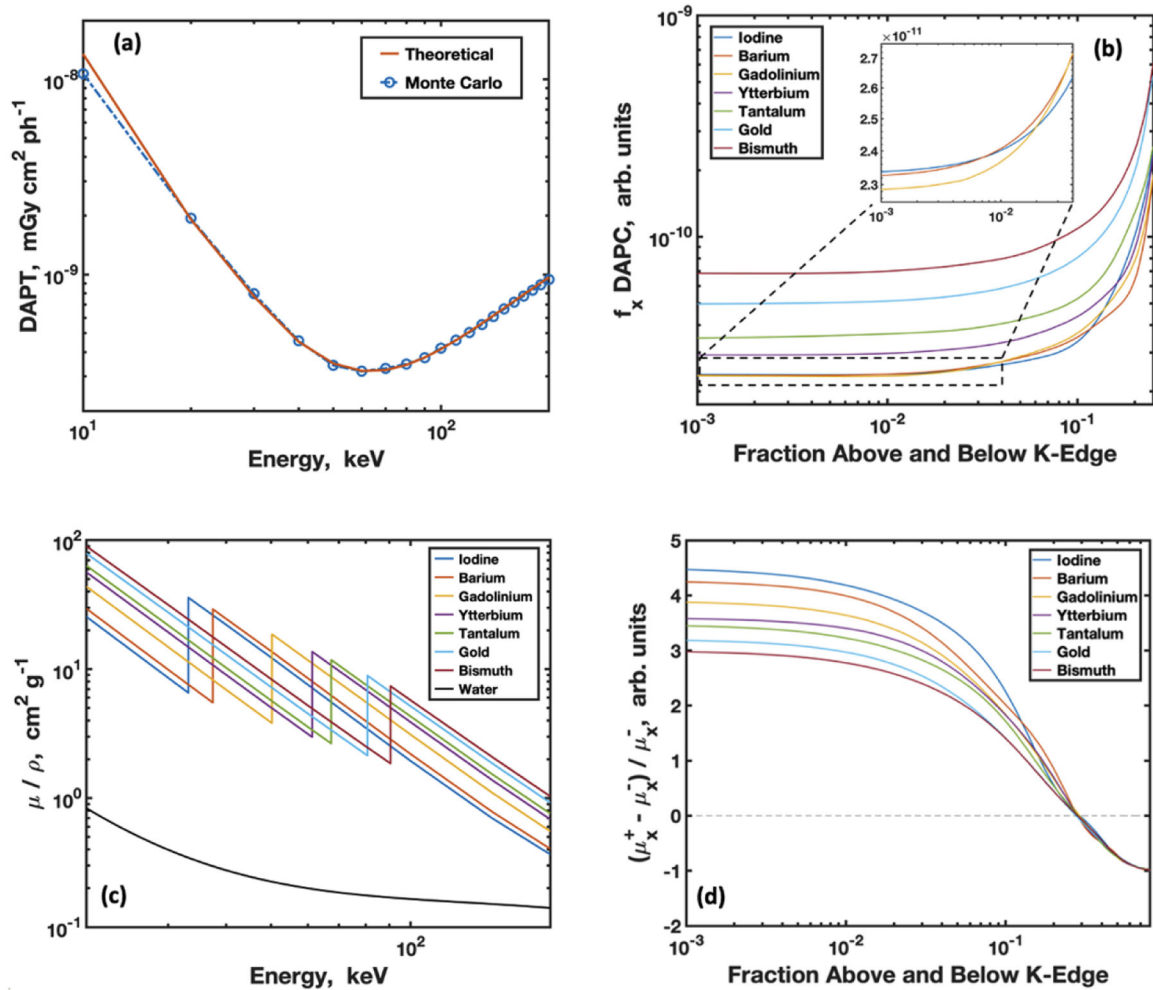
Fig. 2.
(a) Plot relating dose per transmitted photon as a function of energy. Minimization of this curve would yield the energy that simultaneously optimizes low dose and high counting statistics (approximately 60 keV). (b) DAPC curves for various contrast agents; inset – zoom on overlapping curves for I, Ba and Gd. DAPC was multiplied by f_x to remove its dependence on the amount of contrast material. The units are fundamentally arbitrary as the contrast can be defined in unique ways. (c) Plot of mass attenuation coefficient as a function of energy around the K-edge of the contrast elements. (d) Relative change in attenuation coefficient around the K-edge energy.
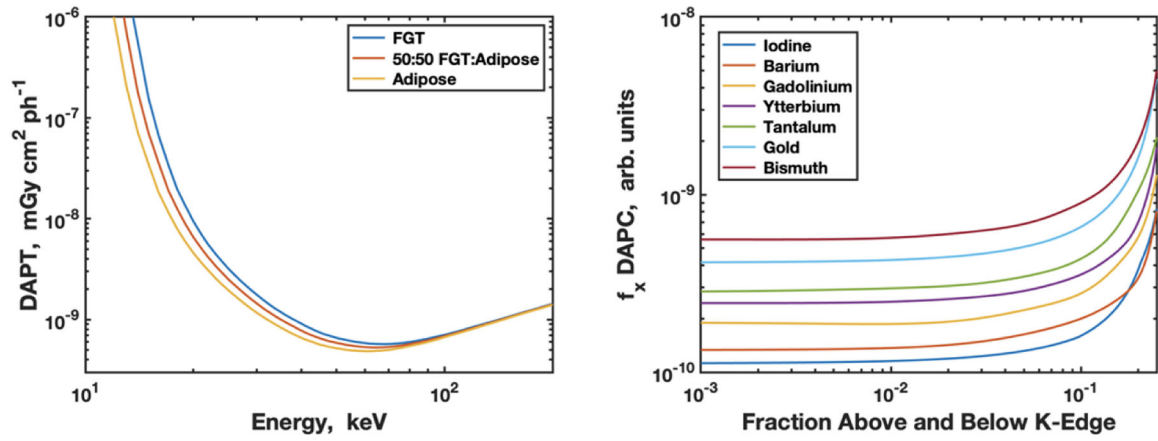
Fig. 3.
(a) DAPT as a function of energy for 50:50 FGT:adipose. Pure FGT and pure adipose simulations are included for reference. (b) DAPC curve for 50:50 FGT:adipose.
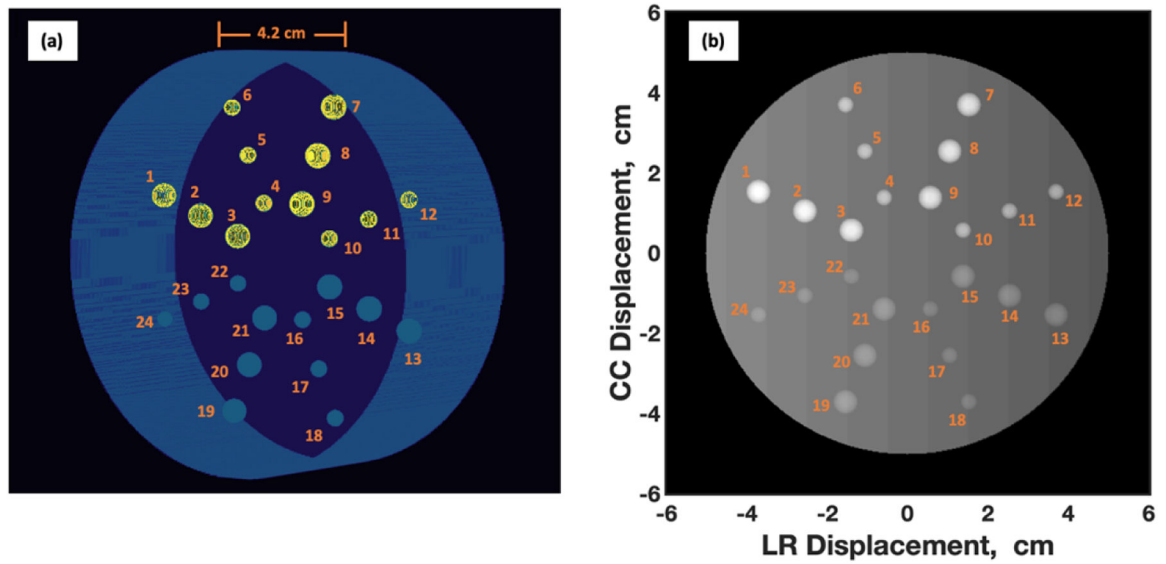
Fig. 4.

(a) 3-dimensional render of the computational phantom used for code verification with insert numbers. The phantom has 4.2 cm depth with a 5 cm radius. Spherical inserts are centered to mid-depth in the phantom and have radii of 2 and 3 mm. Yellow inserts are the large concentration inserts while the light blue ones are the low concentration inserts. (b) Image of phantom used in KES and conventional simulations illustrating the variation in fibroglandular tissue density. There are 11 different fibroglandular tissue fractions ranging from 100% (far left band) to 0% (far right band) in equal increments with 50% being the middle band. Otherwise, the sizes of the phantom and inserts are the same as (a). (CC = craniocaudal, LR = left-right lateral)
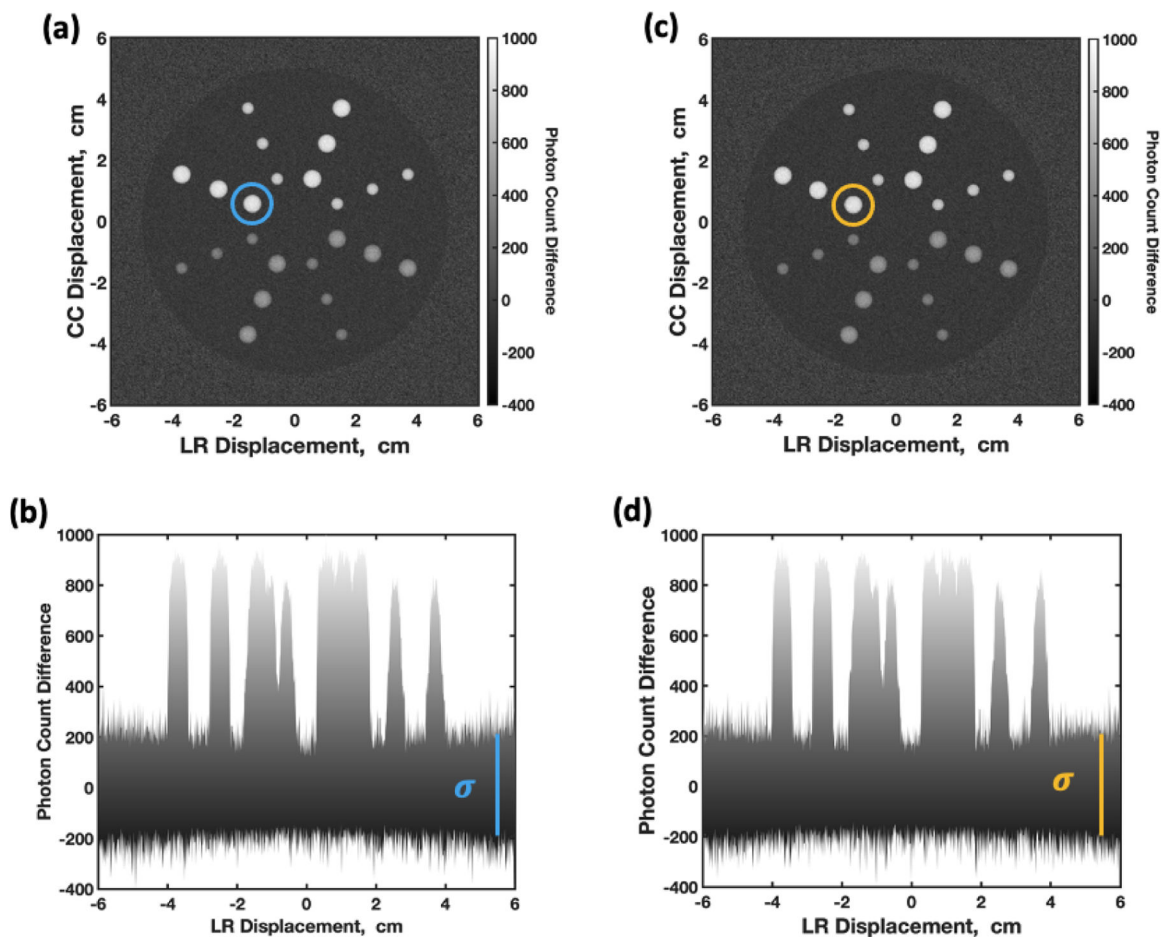
Fig. 5.
KES images comparing MC, images (a) and (b), to the BL code, images (c) and (d). Signal of intensities of circled inserts are 861 (blue, MC) and 851 (yellow, BL) having a difference of only 1.2%. The standard deviation (σ, noise) of the background for these images were 92.6 (blue, MC) and 93.6 (yellow, BL) yielding a difference of 1.1%. (CC = craniocaudal, LR = left-right lateral)
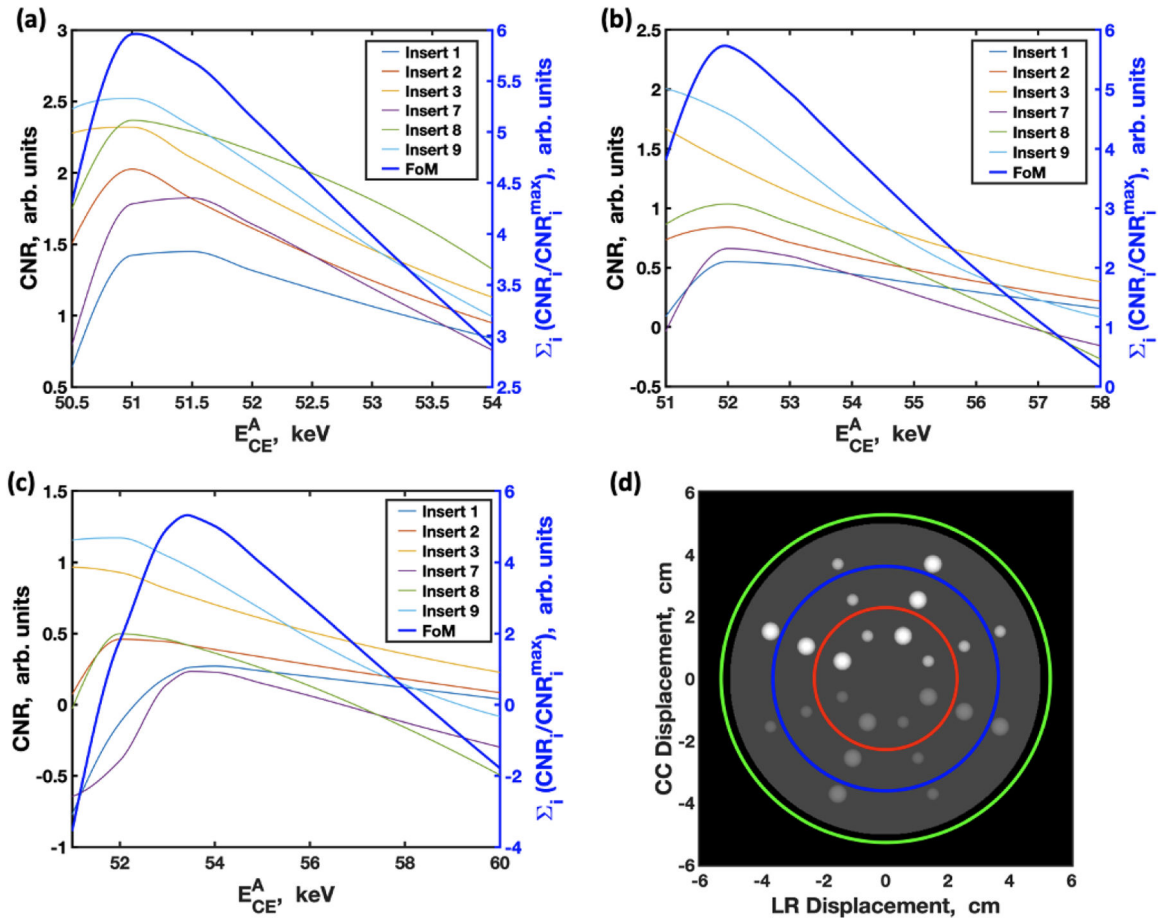
Fig. 6.

FoM curves with individual insert CNRs for 2% (a), 6% (b) and 11% (c) bandwidth LCS sources. The peaks of the FoM curves (blue) yield the best maximum AKE energies to use at each bandwidth. Image (d) shows the mean energies contours at the K-edge of Gd (50.2 keV) for the AKE spectrum overlayed with the phantom for the 11% bandwidth case. The rings tend outward as the energy of the electron beam increases. The best FoM would be the energy that is just high enough to encompass all the inserts, as is predicted from the formula. AKE energies used for the mean energy contours in (d) are 51 keV (red), 52 keV (blue) and 54 keV (green).
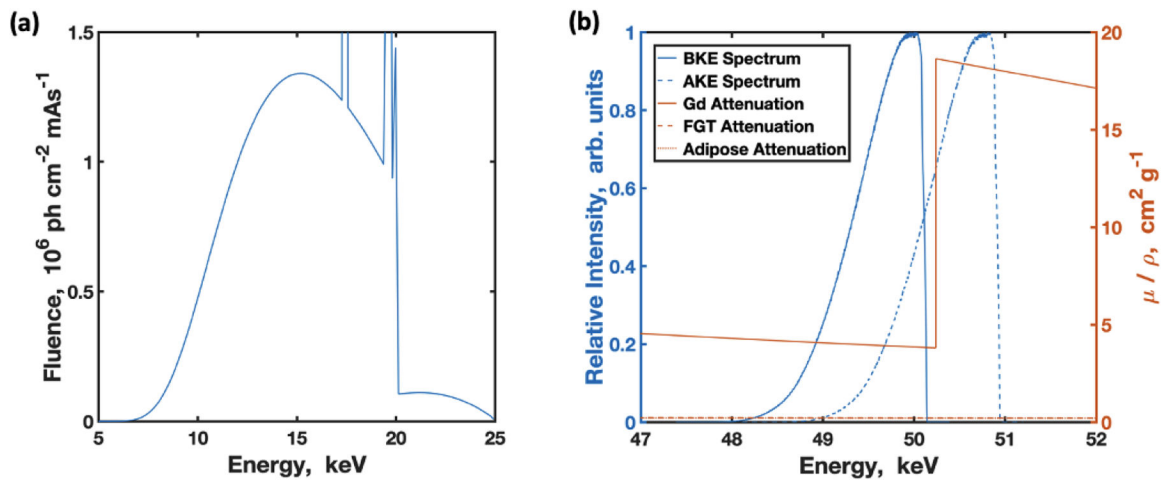
Fig. 7.
Integrated energy spectra for (a) 25 kVp Mo-Mo bremsstrahlung and (b) 2% BW LCS sources used in simulations overlayed with the X-ray mass attenuation coefficient for Gd, FGT and adipose tissue.
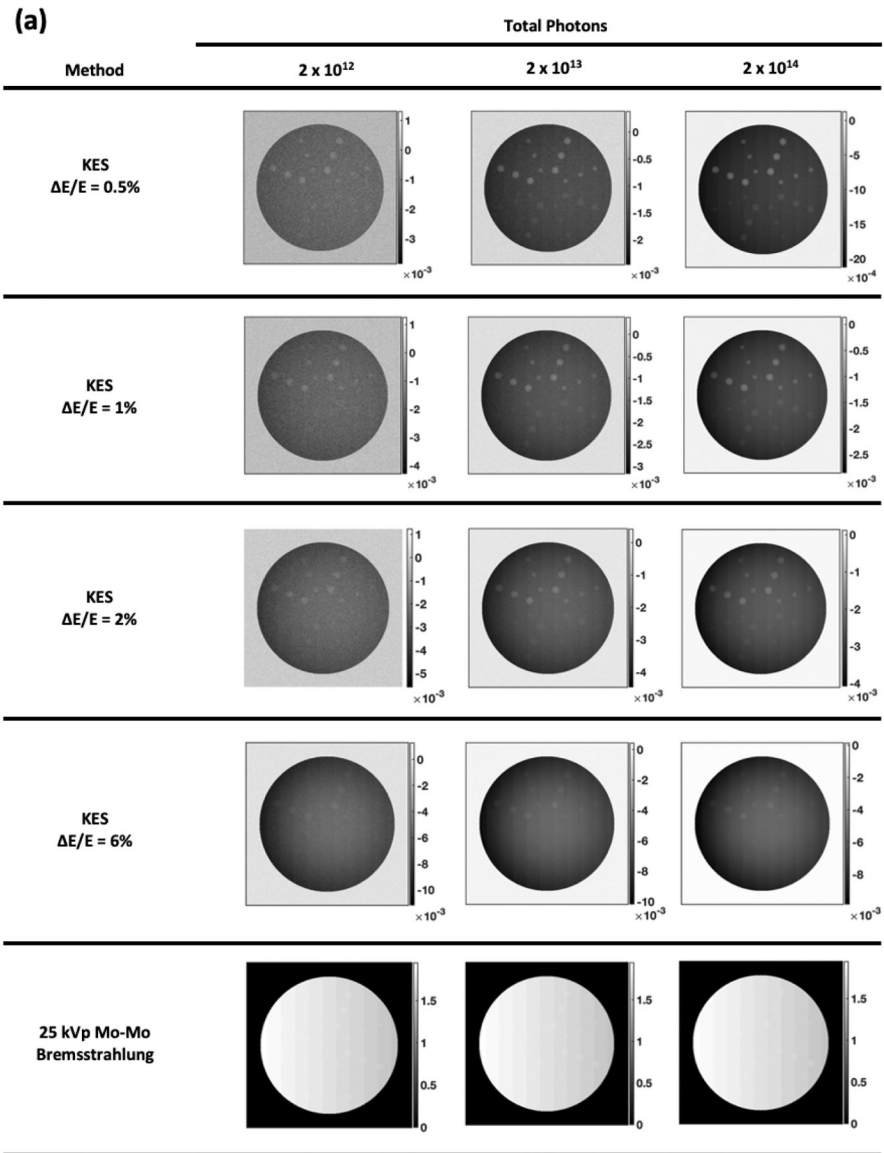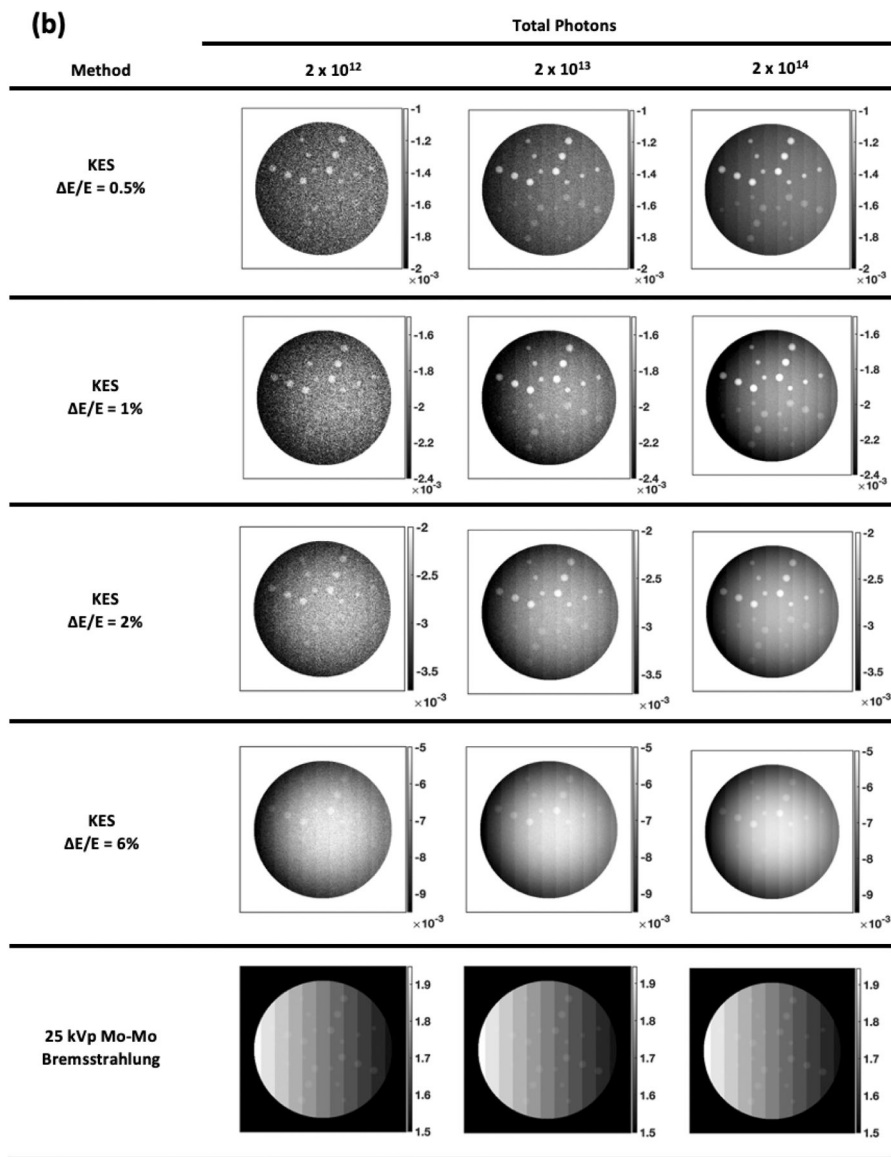
Fig. 8.
KES images obtained for 0.5%, 1%, 2% and 6% BW at a flux of 10^{12}, 10^{13} and 10^{14} ph/projection, as well as the corresponding bremsstrahlung (conventional) images at the same number of photons per image. (a) Displays the raw images without post-processing while (b) shows images with arbitrary thresholds applied to the upper and lower bounds of the signal. Color bars for the KES images represent the difference in the log photon count after adjusting for flux while for the bremsstrahlung images represent the absorption (log-attenuation).
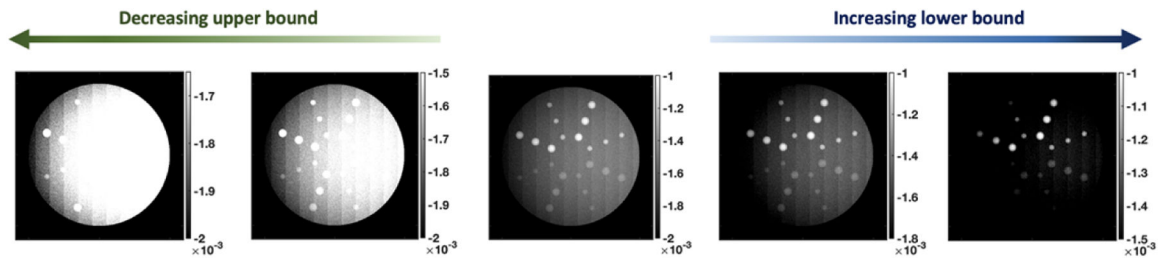
Fig. 9.

0.5% BW KES simulation at 10^{14} ph/projection with various thresholding. Thresholding is a common post-processing technique in medical imaging and can be used to highlight different features of the phantom.

Table 1.

LCS Parameters of the Source Under Construction at Lumitron Technologies, Inc.

Electron Beam Parameters		Laser Parameters	
Micro-bunch charge	25 pC	Laser micro-pulse energy	10 mJ
Pulse structure	1000 micro-bunches/pulse	Laser wavelength	354 nm
Repetition rate	400 Hz	Repetition rate	400 Hz
e^- beam energy	30 – 100 MeV	Laser pulse duration	2 ps
e^- beam energy spread	0.03%	Laser beam spot size	> 5 μm
RF	11.424 GHz		
e^- beam emittance	0.2 mm mrad	**X-ray Characteristics**	
e^- beam size at the interaction point / spot size (RMS)	5 μm	Total X-ray flux	$> 10^{12}$ ph s^{-1}
e^- bunch length	2 ps	Tunable energy range	30 keV – 3 MeV
		X-ray spot size (RMS)	5 μm
Interaction angle	π (head-on)	Minimum on-axis energy bandwidth (E/E, FWHM)	10^{-3}

Table 2.

List of FDA-approved GBCAs

GBCA	Type	Excretion	Concentration (M)	Recommended dose (mmol kg^{-1})
Gadopentetate dimeglumine	linear, ionic	renal	0.5	0.1
Gadobenate dimeglumine	linear, ionic	95–96% renal 4–5% hepatic	0.5	0.1
Gadodiamide	linear, non-ionic	renal	0.5	0.1
Gadoterate meglumine	cyclic, ionic	renal	0.5	0.1
Gadoteridol	cyclic, non-ionic	renal	0.5	0.1
Gadobutrol	cyclic, non-ionic	renal	1.0	0.1

Table 3.

Estimated MGD for LCS at Various Bandwidths and the Conventional Source

Method	KES E/E = 0.5%	KES E/E = 1%	KES E/E = 2%	KES E/E = 6%	KES E/E = 11%	25 kVp Mo-Mo Bremsstrahlung
MGD (10^{-12}mGy ph^{-1})	3.56	3.58	3.61	3.74	3.92	4.16

Table 4.

Insert Group Contrast and Dose Analysis

Photons per Image	Simulation	Insert Group	Mean RCR	Mean CNR	RCRD	CNRD
2×10^{12}	LCS KES, BW = 0.5%	HCLR	0.2254	0.5442	29.34	0.91
		HCSR	0.1530	0.3616	20.39	0.45
		LCLR	0.0684	0.1630	6.90	0.25
		LCSR	0.0471	0.1163	10.69	0.18
	LCS KES, BW = 2%	HCLR	0.1234	0.5098	16.07	0.86
		HCSR	0.0819	0.3341	10.92	0.41
		LCLR	0.0347	0.1428	3.50	0.22
		LCSR	0.0248	0.1051	5.63	0.17
	LCS KES, BW = 6%	HCLR	0.0481	0.4345	6.26	0.73
		HCSR	0.0299	0.2843	3.99	0.35
		LCLR	0.0092	0.0843	0.93	0.13
		LCSR	0.0087	0.0822	1.97	0.13
	25 kVp Mo-Mo Bremsstrahlung	HCLR	0.0090	0.6957		
		HCSR	0.0088	0.9445		
		LCLR	0.0116	0.7568		
		LCSR	0.0051	0.7364		
2×10^{14}	LCS KES, BW = 0.5%	HCLR	0.2245	2.4211	29.24	4.05
		HCSR	0.1531	2.2131	20.41	2.60
		LCLR	0.0690	1.3373	6.95	2.06
		LCSR	0.0467	0.9824	10.61	1.52
	LCS KES, BW = 2%	HCLR	0.1237	1.9532	16.11	3.27
		HCSR	0.0827	1.9072	11.03	2.24
		LCLR	0.0350	0.8940	3.53	1.38
		LCSR	0.0246	0.6667	5.59	1.03
	LCS KES, BW = 6%	HCLR	0.0484	1.0262	6.30	1.72
		HCSR	0.0300	1.0889	4.00	1.28
		LCLR	0.0091	0.2541	0.92	0.39
		LCSR	0.0079	0.2525	1.80	0.39
	25 kVp Mo-Mo Bremsstrahlung	HCLR	0.0090	0.6978		
		HCSR	0.0088	0.9955		
		LCLR	0.0116	0.7585		
		LCSR	0.0051	0.7571		